

Combustion Dynamics Simulation of a 30-Injector Rocket Engine

Juntao Xiong , Feng Liu & William A. Sirignano

To cite this article: Juntao Xiong , Feng Liu & William A. Sirignano (2020): Combustion Dynamics Simulation of a 30-Injector Rocket Engine, Combustion Science and Technology, DOI: [10.1080/00102202.2020.1847097](https://doi.org/10.1080/00102202.2020.1847097)

To link to this article: <https://doi.org/10.1080/00102202.2020.1847097>



Published online: 03 Dec 2020.



Submit your article to this journal [↗](#)



View related articles [↗](#)



View Crossmark data [↗](#)



Combustion Dynamics Simulation of a 30-Injector Rocket Engine

Juntao Xiong, Feng Liu, and William A. Sirignano

Mechanical and Aerospace Engineering Department, University of California, Irvine, California, USA

ABSTRACT

A computational study of the nonlinear rocket-engine combustion instability is presented for an engine with 30 coaxial methane-oxygen injector ports, a choked nozzle, and a combustion chamber. Three combustion chamber lengths of 18 cm, 24 cm, and 30 cm are simulated with differing instability modes depending on length. Computations using a three-dimensional unsteady $k - \omega$ shear-stress transport delayed detached-eddy simulation method provide detailed time-resolved information about the combustion instability. Our flame-index analysis explains why the premixed-flame structures dominate over diffusion flame-structures in the driving mechanism for the instability. This causes the engine to become more unstable as the mixture becomes more fuel rich. Spontaneous longitudinal-mode and tangential-mode instabilities are observed. The oscillation amplitude of the two instability modes vary in alternating fashion during the simulation time. The alternating behavior of the two instability modes can be modified by pulsing the injector mass-flux on the mixture ratio at a particular frequency.

ARTICLE HISTORY



Received 28 July 2020
Revised 3 November 2020
Accepted 3 November 2020

KEYWORDS

Rocket-engine; combustion instability; flame-index

Introduction

Combustion instability in liquid-propellant rocket engines is a phenomenon involving coupling mechanisms between acoustic waves and flames that affect combustion dynamics and combustion instability (Poinsot and Veynante 2011). The acoustic oscillations occur at natural resonant frequencies for the injection-combustor-nozzle configuration and have amplitudes that rise above the level of combustor noise related to vortex shedding. For the combustion instability, flames engage in the resonant interaction and provide oscillatory burning rates that reinforce the acoustic oscillations. Combustion instability has been studied for many decades and is considered in all development programs for new rocket designs because it is an undesired and harmful phenomenon; the resulting large-amplitude pressure oscillation can modify the thrust vector and damage the engine through increased heat transfer to the walls and injector face. Harrje and Reardon (1972) edited an excellent compilation of works during the 1950s and 1960s. Oefelein and Yang (1993) presented a discussion of instability problems of the F-1 rocket-motor. During the early period, the physics of the oscillation were identified by Crocco and Cheng (1953, 1956) for the longitudinal-mode linear instability. They developed the two-parameter (n , τ) coupling between combustion and acoustics for the stability analysis while Sirignano and Crocco

CONTACT William A. Sirignano  sirignan@uci.edu  Mechanical and Aerospace Engineering Department, University of California, Irvine, CA.

© 2020 Taylor & Francis Group, LLC

(1964) and Mitchell, Crocco, and Sirignano (1969) performed nonlinear analyses for spontaneous and triggered longitudinal mode instabilities with shock-waves formation. Later, Zinn (1968) extended the theory for a transverse mode analysis. Two general types of acoustical combustion instability exist according to Culick (2006): driven instability and self-excited instability. Driven instability is more common in solid-propellant rocket engines while self-excited linear and nonlinear instability are common in liquid-propellant rocket engines.

Anderson and Yang (1995) identified the driving and coupling mechanisms of the combustion instability in liquid rocket engine. Linear instability indicates spontaneous instability with only an infinitesimal magnitude disturbance required for initiation. The nonlinear instability indicates triggered instability where a larger-than threshold disturbance is required to trigger the instability. Relevant history of theoretical and experimental research was recently reviewed by Nguyen and Sirignano (2018). The nonlinear dynamics results in complexity for the combustion-instability mechanism. The nonlinear dynamics can involve injector-to-injector interactions as well as interactions with the upstream feed system and manifold. Experimental studies of combustion instability are very challenging because of the expense and the limitation of measurement techniques (Miller et al. 2005; Sisco et al. 2011). With the current computer power and new numerical algorithm development, numerical simulations can describe the combustion instability of complex systems, providing a more complete explanation of the combustion instability mechanism than is obtainable from experimental data. Popov, Sirignano, and Sideris (2015); (2017)) established new numerical models describing different phenomena in combustion instabilities. There are several single-injector and multi-injector studies (Nguyen, Popov, Sirignano 2018; Nguyen and Sirignano 2018; Oefelein and Yang 1998; Urbano et al. 2016). Oefelein and Yang (1998) performed a large-eddy simulation (LES) for a two-dimensional single-injector flow with 24 chemical reactions. Menon and Jou (1991) used LES for study of the combustion instability in an axisymmetric ramjet combustor. Huo and Yang (2017) and Wang et al. (2018a) developed LES for the supercritical combustion. Wang et al. (2018b) (2018b) performed the supercritical combustion LES simulation for the staged-combustion engines. Nguyen, Popov, and Sirignano (2018) and Nguyen and Sirignano (2018) developed a highly efficient solver with the delayed detached-eddy simulation and the compressible flamelet-progress-variable model. The flamelet model is built around the assumption of quasi-steady diffusion control. The flame dynamics occur across three different stability regimes: unstable, semi-stable, and stable. Urbano et al. (2016) performed LES for a hydrogen-oxygen liquid-rocket engine with 42 coaxial injectors, addressing two experimental operating conditions investigated at the DLR, German Aerospace Center laboratory. A pressure disturbance with a first transverse modal distribution was superimposed on the steady-state solution with the oscillation quickly dissipating for a small pressure disturbance. However, when a pressure disturbance greater than a threshold is applied, the oscillation reaches a limit cycle. A previous computational study addressed the nonlinear combustion instability of an engine system with a choked nozzle, a combustion chamber, and 10 or 19 coaxial injector ports (Xiong et al. 2020). Jensen, Dodson, and Claflin (1989) evaluated hydrocarbon fuels, such as methane, with liquid oxygen (LOX) considering combustion stability and performance behavior of a rocket engine with 82-injectors. First mode of tangential combustion instability with frequency 5100 Hz was observed under some fuel/oxidizer ratio conditions. To understand better the stability of the reacting flow in

a multiple-injection rocket-engine combustor and to develop and validate the analytical tool, a computational study for a rocket engine with a higher number of coaxial injector ports, a choked nozzle, and a combustion chamber is performed in this paper. In order to reduce the computational cost, a simplified geometry with 30-injector combustor is designed for the combustion simulation. The open-source computational fluid dynamics software OpenFOAM is used for this study.

Numerical method

Numerical solver

In this study, OpenFOAM is used to solve the compressible Navier-Stokes equations which can be expressed as follows:

$$\frac{\partial \rho}{\partial t} + \frac{\partial(\rho u_j)}{\partial x_j} = 0 \quad (1)$$

$$\frac{\partial(\rho u_i)}{\partial t} + \frac{\partial(\rho u_i u_j)}{\partial x_j} = \frac{\partial(\tau_{ij})}{\partial x_j} - \frac{\partial p}{\partial x_i} \quad (2)$$

$$\frac{\partial(\rho E)}{\partial t} + \frac{\partial(((\rho E) + P)u_j)}{\partial x_j} = \dot{\omega}_T - \frac{\partial q_i}{\partial x_i} + \frac{\partial(\sigma_{ij}u_i)}{\partial x_j} \quad (3)$$

where the viscous stress tensor τ_{ij} is given by

$$\tau_{ij} = \tau_{ij}^L + \tau_{ij}^T \quad (4)$$

$$\tau_{ij}^L = \mu \left(\frac{\partial u_i}{\partial x_j} + \frac{\partial u_j}{\partial x_i} \right) - \frac{2}{3} \mu \frac{\partial u_k}{\partial x_k} \delta_{ij} \quad (5)$$

$$\sigma_{ij} = \tau_{ij} - p \delta_{ij} \quad (6)$$

The Detached-Eddy Simulation (DES) (Strelets 2001) model based on the $k - \omega$ shear-stress transport (SST) (Menter 1994) is used for turbulence closure.

The $\dot{\omega}_T$ represents the heat release rate due to combustion, and q_i represents the energy flux and is given by

$$q_i = -\lambda \frac{\partial T}{\partial x_i} + \rho \sum_{k=1}^{NS} h_k Y_k V_{k,i} \quad (7)$$

where $V_{k,i}$ represents the diffusion velocity and is defined as

$$V_{k,i} = -\frac{D_k}{X_k} \frac{\partial X_k}{\partial x_i} \quad (8)$$

The species transport equation is

$$\frac{\partial(\rho Y_k)}{\partial t} + \frac{\partial(\rho u_j Y_k)}{\partial x_j} = \frac{\partial}{\partial x_j} \left(\rho D_k \frac{W_k}{W} \frac{\partial X_k}{\partial x_j} \right) + \dot{\omega}_k; \quad k = 1, \dots, NS \quad (9)$$

where W_k is the species molecular weight, W is the total molecular weight, D_k is the coefficient of species diffusion, and $\dot{\omega}_k$ is the generation of species due to chemical reaction. The Westbrook–Dryer one-step global reaction for methane and oxygen is used to calculate the generation of species due to chemical reactions and the heat release rate. No turbulent combustion closure is included. The reacting-mixtures model is used to calculate the properties of the mixtures. More details about the numerical models are given in the publication (Xiong et al. 2020).

The OpenFOAM 4.0 combustion simulation solver rhoReactingFoam is used for the compressible combustion simulation with chemical reaction. The differencing schemes used are second-order accurate in both space and time. The time discretization is second-order implicit backward differencing. Gaussian integration is used for the spatial discretization with linear interpolation from cell centers to cell faces for second-order derivatives. The ideal-gas state equation is used in this paper for simplicity. The specific heat c_p is calculated as a function of temperature from the JANNAF tables of thermodynamics.

Computational mesh

A 30-injector rocket engine combustor is configured to mimic an experimental 82-injector rocket engine combustor (Jensen et al., 1989) in this study. A computational model with 30 injectors is used to avoid the high cost for an 82-injector combustion analysis. The experiment model (Jensen et al., 1989) had a chamber length of 24 cm. In addition to that length, we examine a shorter length (18 cm) and a longer length (30 cm) as well in the present study. Figure 1 shows the 30-injector and 82-injector combustor geometries. The combustion chamber diameter is 14.38 cm. P1-P6 marks six pressure probes around the combustion chamber wall. Figure 2 shows the combustor geometry. The fuel and oxygen were injected with coaxial injectors. The D_{ox} is 6.62 mm and D_{fuel} is 7.505 mm. The length of the injector is 30 mm. The individual co-axial injection for the 30-injector design matches

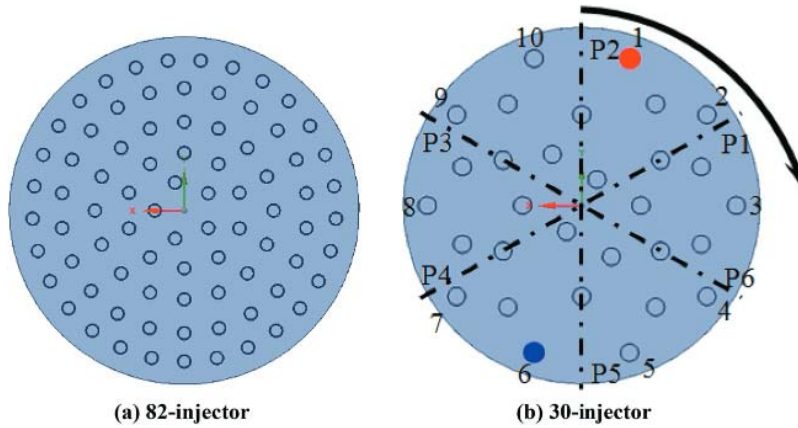


Figure 1. Front view of the injector plate.

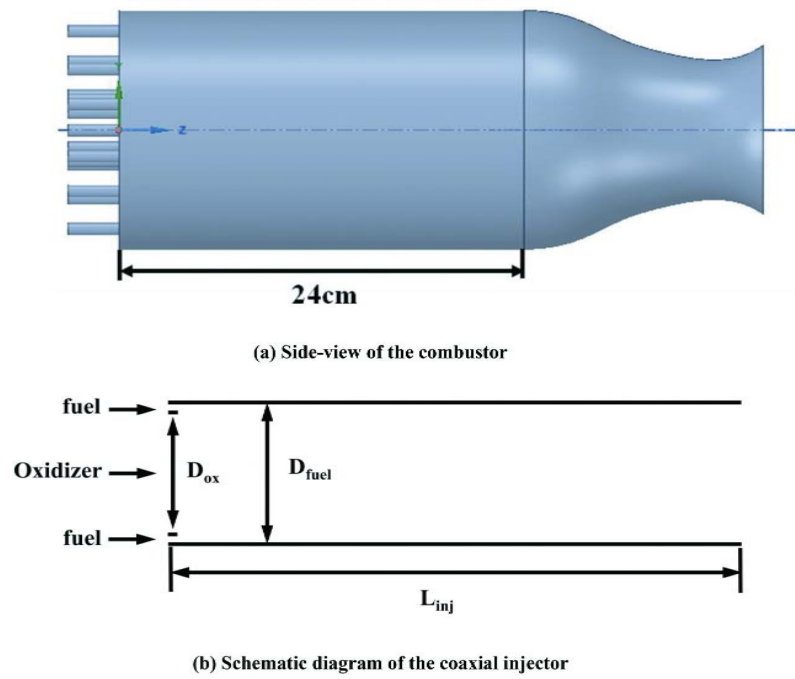


Figure 2. Geometry of 30-injector combustor.

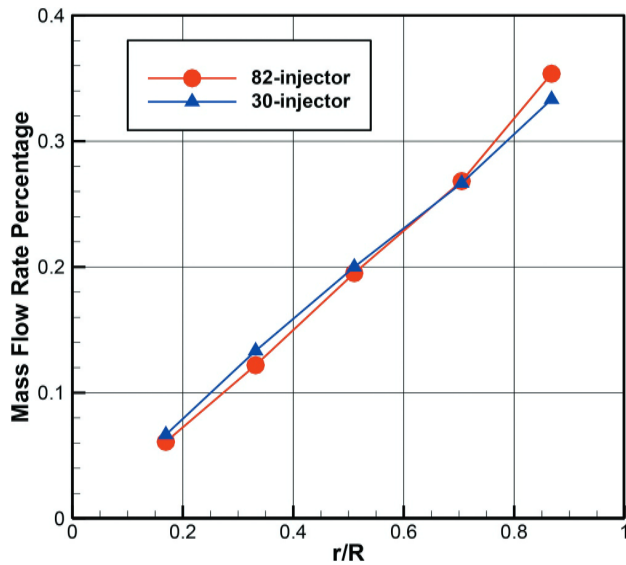


Figure 3. Inlet mass flow rate radial distributions.

the injection geometry for the 82-injector engine. The radial distribution of the inlet mass flow rate of the 30-injector combustors is designed to match that of the 82-injector combustor. Figure 3 shows the comparison of the radial distributions. In the simulation,

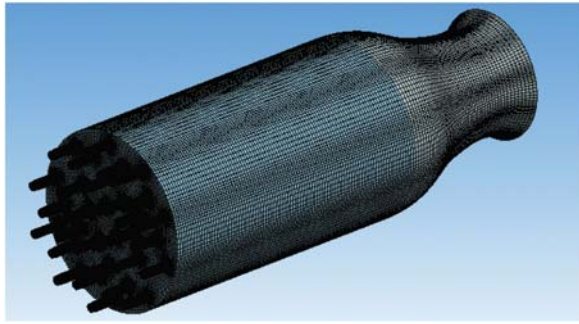


Figure 4. Computational mesh.

the total mass flow rate and the mixture ratio match those in the experiments. So, the solution for 30-injectors is expected to be similar to that of the 82-injector combustor. [Figure 4](#) shows the unstructured mesh for the 30-injector combustor. A grid independency study had been performed for a combustion chamber with 19-injector case in the publication (Xiong et al. 2020). The results show that overall qualitatively good grid-independent solutions were achieved on both coarse and fine meshes. The similar pressure oscillation frequencies and instability behaviors were captured on both coarse and fine meshes. In this paper, the same smallest mesh size 0.02 cm as the 19-injector combustion chamber fine mesh is used for the 30-injector combustion chamber. The total number of nodes is about 12.1 million for the 24 cm length combustion chamber.

Boundary conditions

Along the wall, the no-slip boundary condition is used. The normal pressure gradient on the wall is zero. Adiabatic walls with no surface chemistry are assumed. In the injector ports, the mean mass fluxes for methane and oxygen are fixed to yield the steady-state mass flow rate at the sonic point for the convergent nozzle. The wave-transmissive boundary condition is used at the outlet boundary because of the supersonic nozzle flow. This boundary condition ensures that no backward propagating waves enter the system to avoid occurrences of shocks or backflow in the combustion.

Jensen, Dodson, and Claflin (1989) tested the 82-injector engine combustion instability over a range of conditions; we only treat some of those conditions. Their report lists those cases as test numbers 019, 027, and 032. In two of those tests, the experiment gave a first-tangential instability at a frequency of about 5100 Hz. The other case was stable. The three imposed flow conditions are listed in [Table 1](#). The experimental observations at the three conditions are listed in [Table 2](#).

Results

The simulations only consider the gas phases of the methane and oxidizer and use the ideal-gas equations of state, which might introduce some errors at the very high pressures. Qualitatively similar results to the Rocketdyne test results from Jensen, Dodson, and

Table 1. Imposed flow conditions.

	Case1	Case2	Case3
Mixture ratio	2.53	3.38	3.69
Velocity ratio	11.0	8.8	5.6
Momentum ratio	4.31	2.58	1.51
\dot{m}_{fuel} (lb/s)	24.23	19.56	20.65
\dot{m}_{ox} (lb/s)	61.74	66.77	76.72
T_{fuel} (F)	20.7	47	-10
T_{ox} (F)	-244	-242	-247
ρ_{fuel} (lb/cu.ft)	8.1	7.5	11.1
ρ_{ox} (lb/cu.ft)	64.7	64.6	65.8
V_{fuel} (ft/s)	708	620	444
V_{ox} (ft/s)	64	70	79

Table 2. Experimental observations.

	Case1	Case2	Case3
Instability Mode	Tangential 1 T	Tangential 1 T	Stable 2015
Frequency	5100 Hz	5100 Hz	
Chamber Pressure (psia)	1886	1960	2127

Table 3. Parameters of the computation cases.

	Lc(cm)	Longitudinal Mode	f_L	Tangential Mode	f_T	Ta (K)
Case1	24	1 L	2063	1 T	4550	3916
Case2	24	1 L	2015	1 T	4611	4112
Case3	24	-	-	-	-	4235

Clafin (1989) are obtained in the computational simulations, as are shown in Tables 2 and 3. Namely, the first tangential-mode instability is weakened as the mixture ratio is increased and moved toward the stoichiometric value.

Different mass mixture ratios and combustion chamber lengths are simulated in this study. The impact of short-duration pulsing of the flow of a few injectors is studied. Cases 1, 2, 3 address three different mixture ratios described in Table 1 for the 24 cm long combustion chamber. The fuel-rich mixture moves closer to stoichiometry as progress is made from Case 1 to Case 3. Case 1b addresses an 18 cm chamber with the mixture conditions of Case 1; Case 1 c applies to the 30 cm chamber.

For the chamber length of 24 cm and diameter of 14.38 cm, the spontaneous oscillations include both the first tangential mode at roughly 4500 Hz and the first longitudinal mode at roughly 2000 Hz. The amplitudes of the two modes increase and decrease alternately over periods of milliseconds (i.e., many cycles) with one mode increasing in amplitude and becoming dominant while the other mode decreases. Thus, energy transfers between the modes in an alternating fashion. As the propellant mixture becomes less fuel rich, the oscillations essentially stabilize by decreasing to the noise level. Sirignano and Crocco (1964) explained why that counter-intuitive result can happen for a combustor where chemical kinetics is rate controlling. It relates to the perturbation of the exponential term where temperature appears in the denominator of the exponent. Consequently, for a given pressure perturbation and thereby a given temperature perturbation, the perturbation in mass burning rate decreases as the mean temperature increases, which happens as the

stoichiometric mixture ratio is approached. The predictions of Sirignano and Crocco were later confirmed by the experiments of Bowman, Glassman, and Crocco (1965). Specifically, they showed the chemical-kinetic-controlled gas rocket became more stable as the mixture ratio moved toward stoichiometry from either the fuel-rich or fuel-lean side. Furthermore, as predicted, the mean temperature at the stability limit was identical on both the fuel-rich and fuel-lean sides. The predicted trend of increasing instability as mixture becomes more fuel rich is also consistent with the findings of Jensen, Dodson, and Claflin (1989).

When the chamber length decreases to 18 cm, the spontaneous tangential mode becomes dominant with little energy for the longitudinal oscillation. Upon pulsing the inflow from two co-axial injectors for a few cycles, maintaining constant total mass flux and mixture ratio, the first longitudinal mode appears together with the first tangential mode. With an increase to the 30-cm length, the tangential mode dominates but a longitudinal mode is present with alternating transfer of energy between the two modes; the tangential mode remains as the dominant mode while the alternating occurs. When the 30-cm chamber is pulsed at 4532 Hz, the longitudinal mode energy level diminishes while the energy level for the tangential mode fluctuates. With pulsing at 3417 Hz, both the longitudinal mode and the tangential mode fluctuate in energy level with the former becoming stronger than it is before pulsing.

24 cm combustion chamber

Simulations of the three cases listed in Table 1 have been made for the 24 cm combustion chamber combustor. The simulations start from an initially quiescent flow at 3000 K and an equilibrium chamber pressure at 200 bar. The higher chamber temperature helps to shorten the ignition process and reduce the computational time without the use of an explicit ignition model in the simulation.

Figure 5 shows the pressure oscillation around the combustor chamber wall at 1 cm downstream from the injection plate for Case 1. Figure 6 shows the FFT analysis of the pressure oscillation at probe 1. Two dominant frequencies, 2063 Hz and 4550 Hz, are observed. The 2063 Hz pressure oscillation corresponds to the first longitudinal mode of combustion instability. The 4550 Hz pressure oscillation indicates the first tangential mode. The peak Power Spectral Density (PSD) for the longitudinal and tangential modes of a series

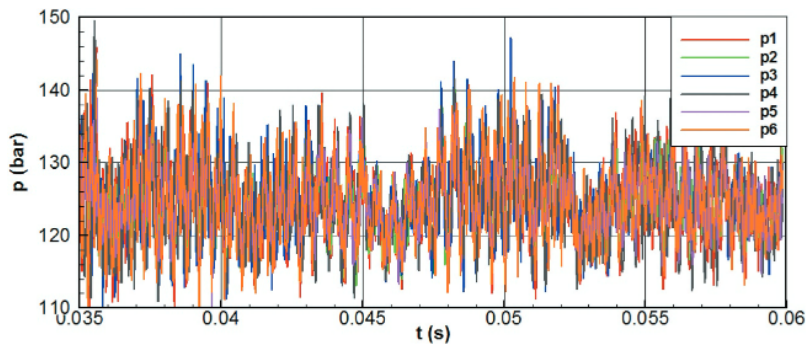


Figure 5. Case 1 pressure history at p1 and p4 on the combustion-chamber wall. ($z = 1$ cm).

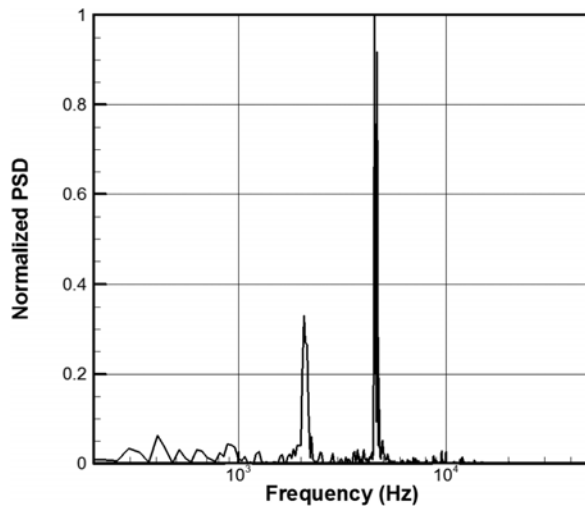


Figure 6. Case 1 FFT of the pressure history at probe p1 on the combustion-chamber wall. ($z = 1$ cm).

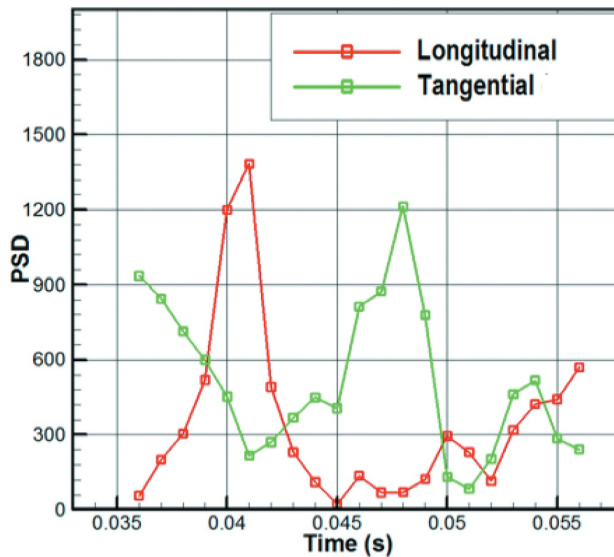


Figure 7. Peak PSD for the longitudinal and tangential modes at probe p1 ($z = 1$ cm).

of consecutive 3 ms duration time window is presented in Figure 7. The strengths of the two modes alternate during the simulation.

Figure 8 shows the pressure oscillation around the combustor chamber wall at 1 cm downstream from the injection plate for Case 2 where the fuel-rich mixture has a new mass ratio closer to the stoichiometric value. The FFT analysis of the pressure oscillation is presented in Figure 9. Two dominant frequencies, 2015 Hz and 4611 Hz, are observed. The 2015 Hz pressure oscillation indicates the first mode of longitudinal combustion instability. The 4611 Hz pressure oscillation corresponds to the first mode of tangential combustion

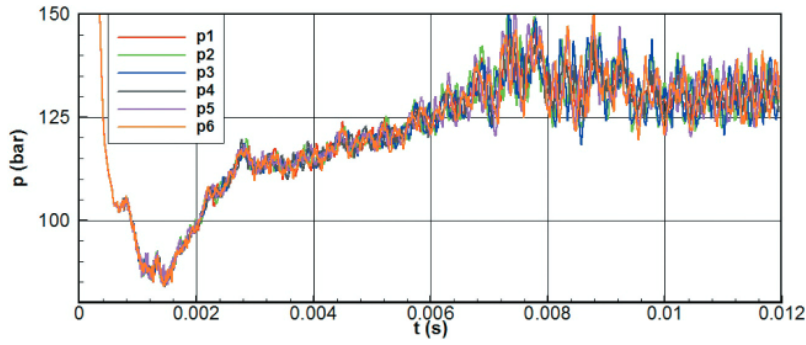


Figure 8. Case 2 pressure history on the combustion-chamber wall. ($z = 1$ cm).

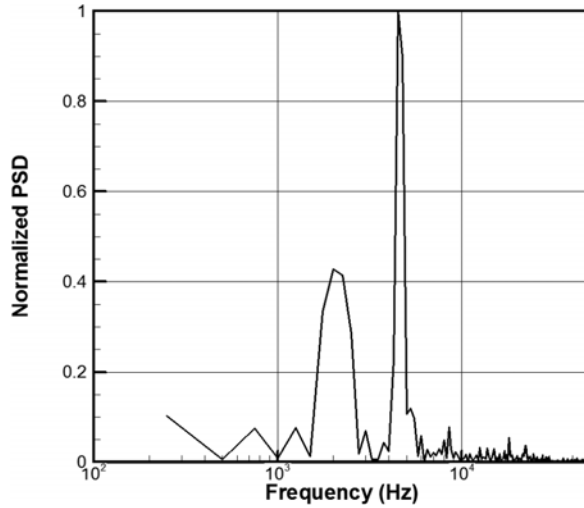


Figure 9. Case 2 FFT of the pressure history at probe p1 on the combustion-chamber wall. ($z = 1$ cm).

instability. With the higher mixture ratio, this case has a smaller amplitude than found in Case 1. The lower velocity ratio apparently slows the rate of burning. As discussed above, Sirignano and Crocco (1964) have shown that oscillation in burning rate can be reduced as the mixture comes closer to stoichiometric value if chemical kinetics is rate controlling.

Figure 10 shows the pressure oscillation around the combustor chamber wall at 1 cm downstream from the injection plate Case 3. The flow is relatively stable. The peak-to-peak pressure oscillation is less than 5% of the mean pressure.

To characterize the flame properties, a simple flame index is defined as heat release rate per unit volume masked by the sign of the dot product of the gradient of the oxygen mass fraction and the gradient of the fuel mass fraction, i.e.,

$$FI = HRR \cdot \text{sign}(\nabla(CH_4) \cdot \nabla(O_2)) \quad (10)$$

where HRR is heat release rate per unit volume. If the index is positive, fuel and oxygen diffuse in the same direction indicating a premixed flame. If the dot product is negative, the

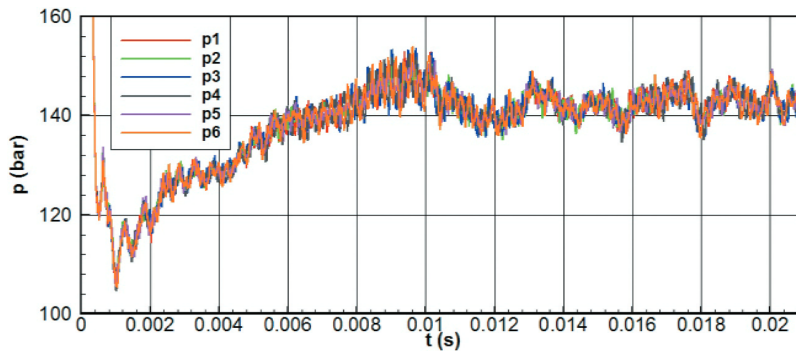


Figure 10. Case 3 pressure history on the combustion-chamber wall. ($z = 1$ cm).

oxygen and fuel diffuse in opposing directions indicating a diffusion flame. The chemical kinetics are more likely to affect the burning rate for a premixed flame and unlikely to affect the burning rate for a diffusion flame. Figures 11 and 12 present the instantaneous contours of the flame index on two meridian planes and two cross-sectional planes for the three cases. The dark red indicates premixed flames and the dark blue indicates diffusion flames. Premixed flames dominate upstream near the injectors and diffusion flames dominate farther downstream in the chamber for the three cases. The tangential mode has its largest amplitude near the injectors so that its interaction with the premixed flames can be expected to be more consequential than its interaction with the diffusion flames. And the pressure antinode of the longitudinal mode occurs also near the injector so that its interaction with the premixed flames can be expected to be more consequential than its interaction with the diffusion flames. Most of the combustion has been completed by the downstream position of the other pressure antinode near the nozzle. The consequential role of the premixed flame explains how the engine becomes more stable as the mixture ratio moves toward the stoichiometric value and the flame temperature increases. The fuel-rich mixture moves closer to the stoichiometric value as progress is made from Case 1 to Case 3. As the propellant mixture becomes less fuel rich, the combustion efficiency and the chamber temperature increase. The oscillations essentially stabilize by decreasing to the noise level. The 82-injector configuration of Jensen, Dodson, and Claflin (1989) has smaller-diameter jets than considered here. So, their mixing times can be expected to be shorter and the dominance of premixed flames can be expected to be greater. The computational results are qualitatively similar to the Rocketdyne test results from Jensen, Dodson, and Claflin (1989) for the 82-injector engine.

18 cm combustion chamber

Now, we consider a shorter chamber length with the same mixture condition of Case 1. We designate this case as Case 1b. Figure 13 shows the pressure oscillation around the combustor chamber wall at 1 cm downstream from the injection plate for this case. The FFT analysis of pressure oscillation is presented in Figure 14. Only one dominant frequency of 4528 Hz is observed, which indicates the first mode of tangential combustion instability.

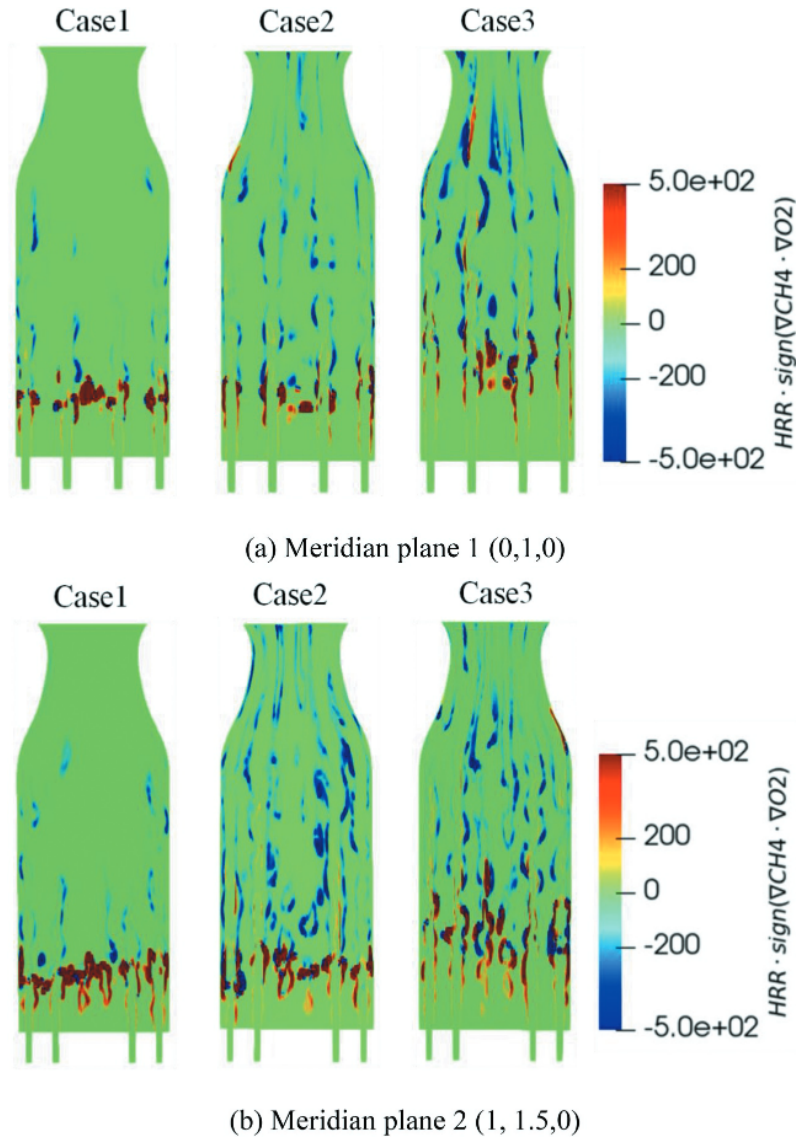


Figure 11. Instantaneous flame index on the chamber meridian planes.

The modulus of the FFT is shown in Figure 15. The tangential instability mode can be decomposed into two spinning waves as

$$A \cos(\omega t - \theta + \varphi_1) + B \cos(\omega t + \theta + \varphi_2) \quad (11)$$

in which $A = 0.575$, $B = 0.5$, $\varphi_1 = 0.0^\circ$, $\varphi_2 = 60.0^\circ$.

To investigate the inlet mass flux pulsing effect, two tangential pulsation tests with frequency 4532 Hz and 3417 Hz are performed. These are designated as Case 1bp1 and Case 1bp2, respectively. The pulsing starts at 10 ms and stops after three cycles. The mass flux through the 10 injectors located at the outer ring of the injection plate shown in

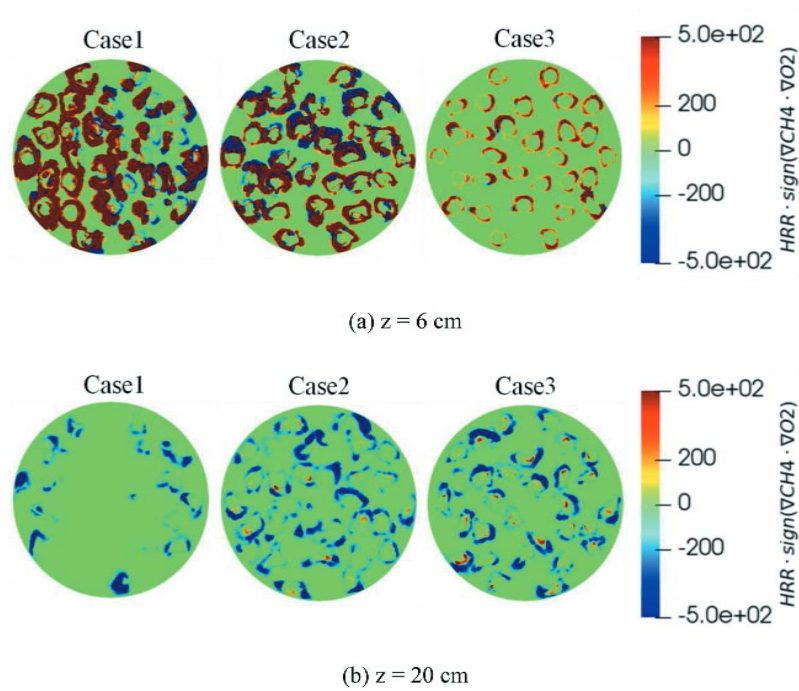


Figure 12. Instantaneous flame index on the chamber cross-sectional planes.

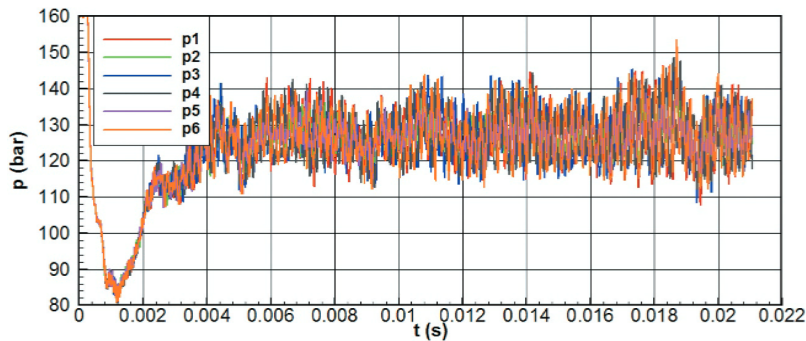


Figure 13. Case 1b pressure history on the combustion-chamber wall. ($z = 1$ cm).

Figure 1b are pulsed at fixed mixture ratio; the mass flux remains steady in the 20 other injectors.

The first inlet mass-flux pulsing frequency is 4532 Hz for Case1bp1. The pressure oscillation around the combustor chamber wall at 1 cm downstream from the injection plate is shown in Figure 16. The FFT analysis of the pressure is presented in Figure 17. Two dominant frequencies, 2273 Hz and 4562 Hz, are observed. The 2273 Hz pressure oscillation corresponds to the first longitudinal combustion-instability mode. The 4562 Hz pressure oscillation indicates the first-tangential combustion instability mode. The inlet mass-flux pulsation could trigger the longitudinal instability for the 18 cm chamber length combustor.

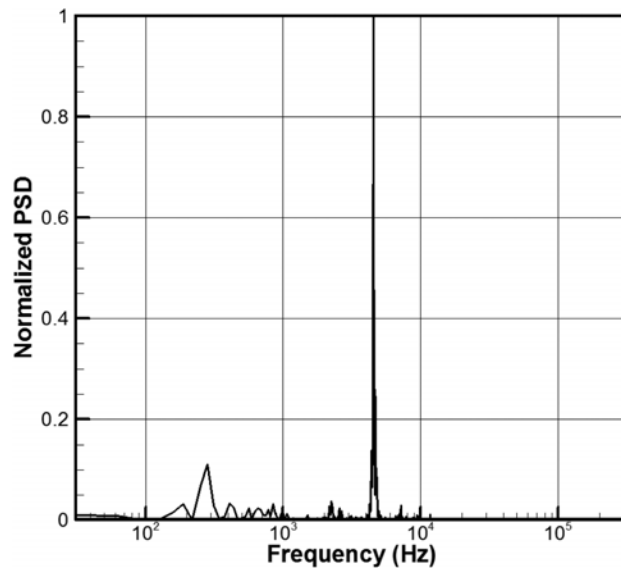


Figure 14. Case 1b FFT of the pressure history at probe p1 on the combustion-chamber wall. ($z = 1$ cm).

The second inlet mass-flux pulsing frequency is Case1bp2 at 3417 Hz. Figure 18 shows the pressure oscillation history. The FFT analysis of the pressure oscillation is shown in Figure 19. The 3417 Hz pulsing introduces a low-frequency pressure oscillation after the

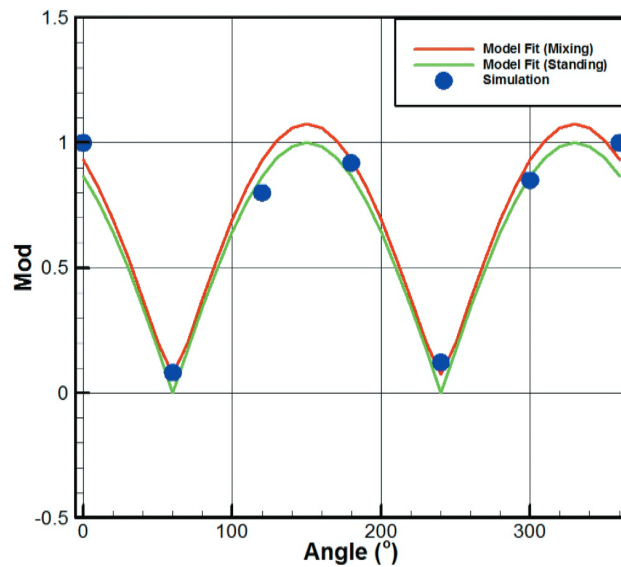


Figure 15. Case 1b normalized modulus of FFT of the pressure history on the combustion-chamber wall. ($z = 1$ cm).

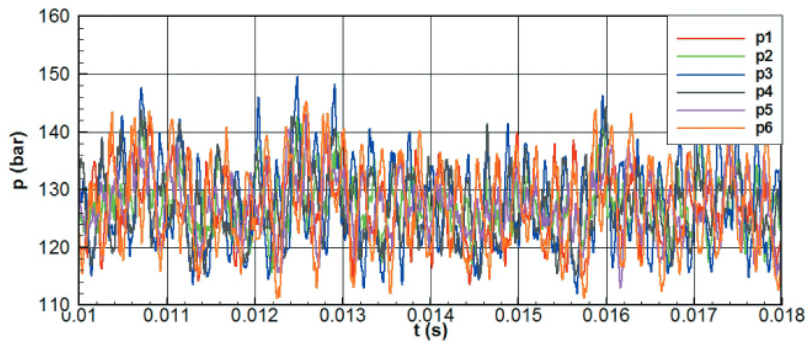


Figure 16. Case 1bp1 pressure history on the combustion-chamber wall for the pulsing frequency 4523 Hz. ($z = 1$ cm).

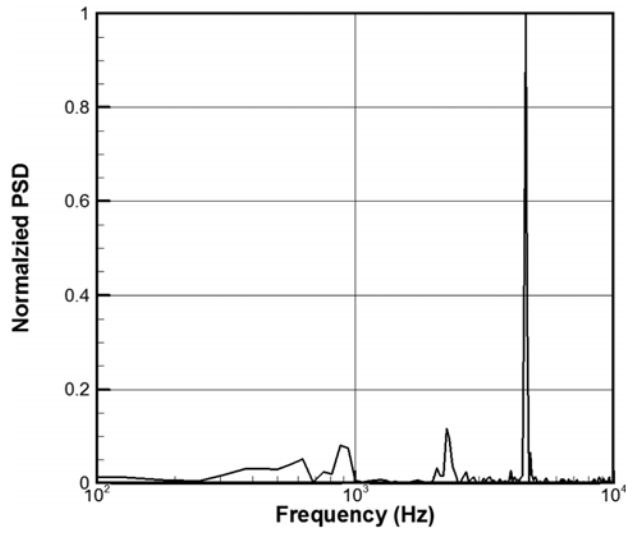


Figure 17. Case 1bp1 FFT of the pressure history at probe p1 on the combustion-chamber wall for the pulsing frequency 4523 Hz. ($z = 1$ cm).

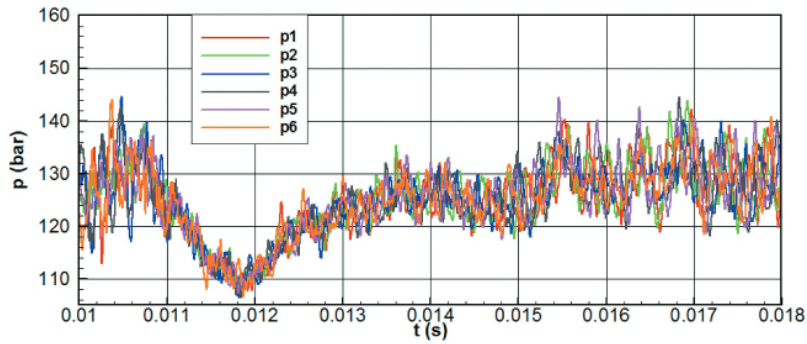


Figure 18. Case 1bp2 pressure history on the combustion-chamber wall for the pulsing frequency 3417 Hz.

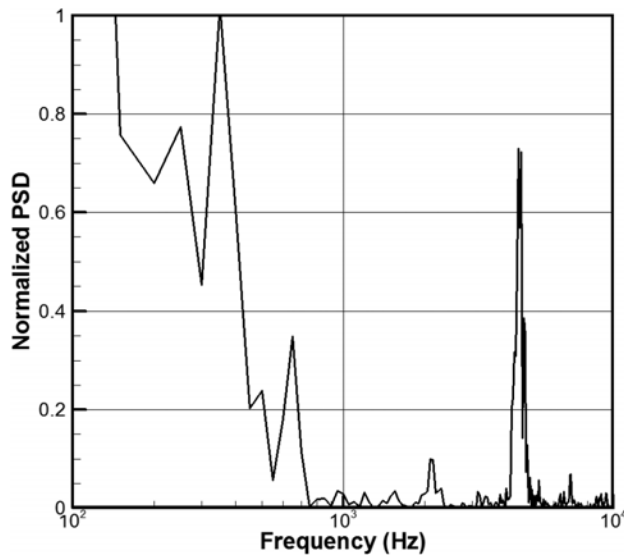


Figure 19. Case 1bp2 FFT of the pressure history at probe p1 on the combustion-chamber wall for the pulsing frequency 3417 Hz. ($z = 1$ cm).

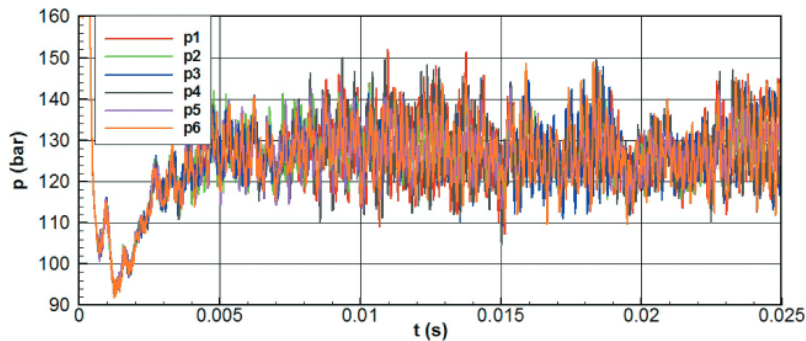


Figure 20. Case 1 c Pressure history on the combustion-chamber wall. ($z = 1$ cm).

pulsation is completed. Overall, the inlet mass flux pulsing results in a less energetic oscillation.

30 cm combustion chamber

Now, a chamber length longer than the experimental case is considered. The pressure oscillation around the combustor chamber wall at 1 cm downstream from the injection plate in Case 1 c is shown in [Figure 20](#). The pressure oscillation FFT analysis is presented in [Figure 21](#). Two dominant frequencies, 2000 Hz and 4654 Hz, are observed. The 2000 Hz pressure oscillation corresponds to the first mode of longitudinal combustion instability. The 4654 Hz pressure oscillation indicates the first mode of tangential combustion instability. [Figure 22](#) shows the peak PSD for the longitudinal and tangential modes. The strengths

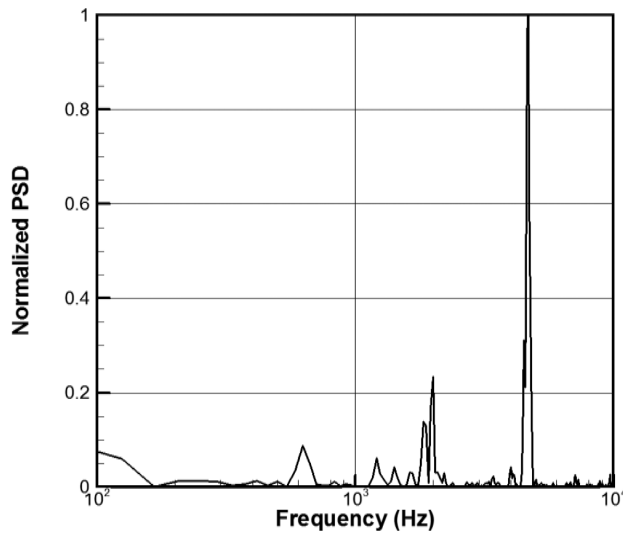


Figure 21. Case 1 c FFT of the pressure history at probe p1 on the combustion-chamber at probe p1. ($z = 1$ cm).

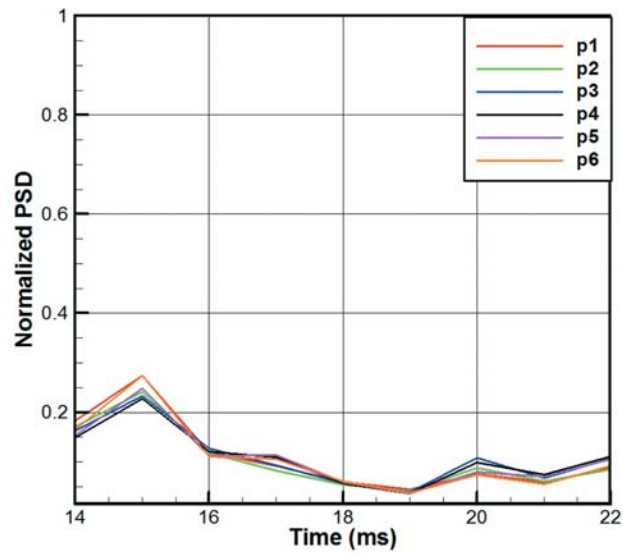
of the two modes alternate during the simulation. The energy contained by the tangential instability is larger than the longitudinal instability. And the strength of the tangential instability oscillates during the simulation time.

30 cm combustion chamber with injector mass-flux pulsing

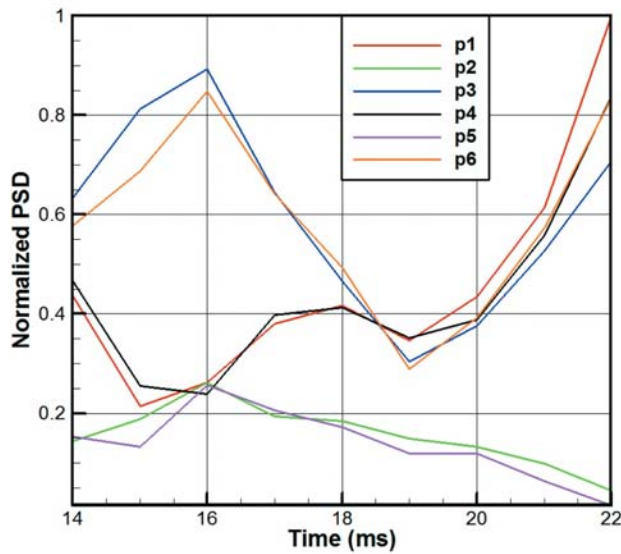
Two tangential pulsation tests with frequencies 4532 Hz and 3417 Hz are performed to investigate the inlet mass flux pulsing effect. The pulsing starts at 10 ms and stops after three cycles.

Figure 23 shows the Case 1 cp1 pressure oscillation around the combustor chamber wall at 1 cm downstream from the injection plate for the inlet mass flux pulsing with frequency 4532 Hz. The FFT analysis of the pressure oscillation is presented in Figure 24. Two dominant frequencies, 1829 Hz and 4582 Hz, are observed. The 1829 Hz pressure oscillation corresponds to the first mode of longitudinal combustion instability. The 4582 Hz pressure oscillation indicates the first mode of tangential combustion instability. The frequencies of the two modes are slightly changed with the pulsing. But the tangential instability still dominates the pressure oscillation. The peak PSD for the longitudinal and tangential modes are shown in Figure 25. With the frequency 4532 Hz inlet mass flux pulsing, the longitudinal instability turns weaker.

The Case 1 cp2 pressure oscillation around the combustor chamber wall at 1 cm downstream from the injection plate for the inlet mass-flux pulsing with frequency 3417 Hz is presented in Figure 26. Figure 27 shows the FFT analysis of the pressure. Two dominant frequencies, 1810 Hz and 4597 Hz, are observed. The 1810 Hz pressure oscillation corresponds to the first mode of longitudinal combustion instability. The 4597 Hz pressure oscillation indicates the first mode of tangential combustion instability. The two-mode frequencies are also slightly altered by the pulsing. But the longitudinal instability is



(a) Longitudinal mode



(b) Tangential mode

Figure 22. Case 1 c peak PSD for the longitudinal and tangential modes ($z = 1$ cm).

significantly enhanced by the 3417 Hz inlet mass-flux pulsing. Figure 28 presents the peak PSD for the longitudinal and tangential modes. With the frequency 3417 Hz inlet mass-flux pulsing, the longitudinal instability turns stronger. The energy contained by the longitudinal and tangential instability oscillate during the simulation time.

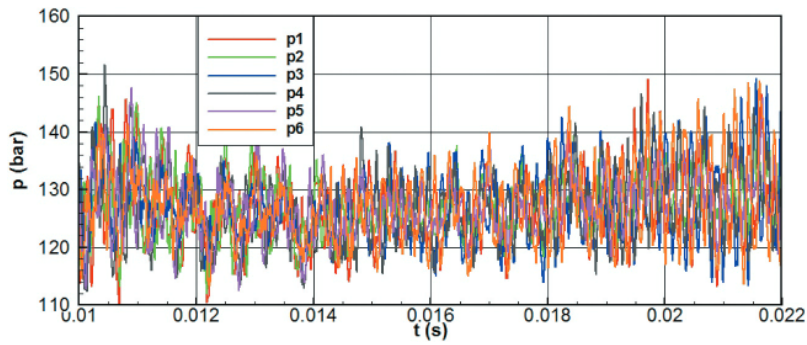


Figure 23. Case 1 cp1 pressure history on the combustion-chamber wall for the pulsing frequency 4532 Hz. ($z = 1$ cm).

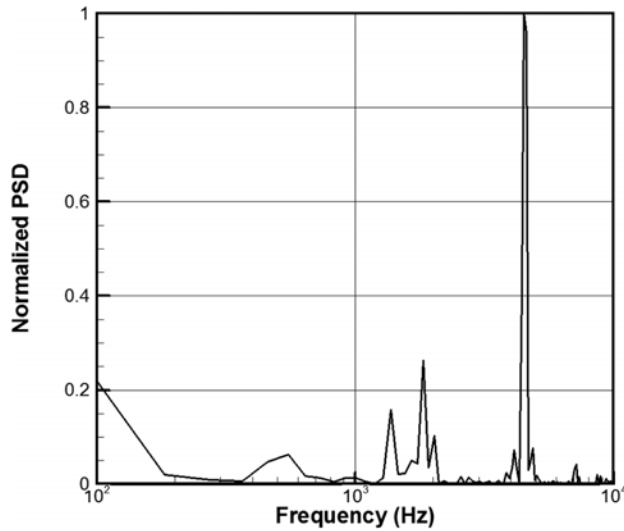
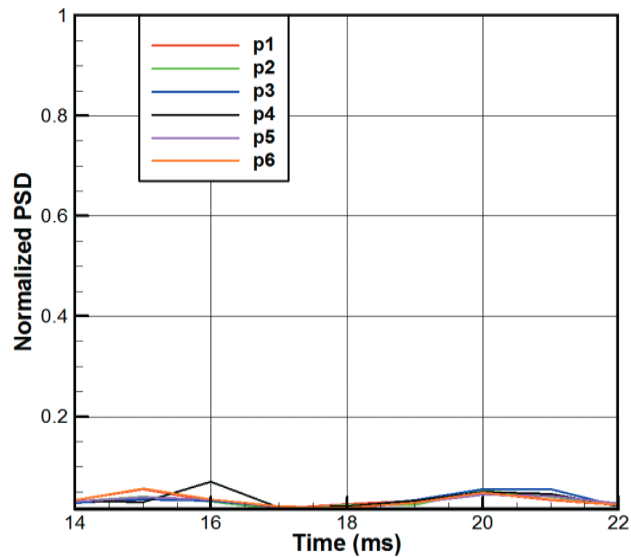


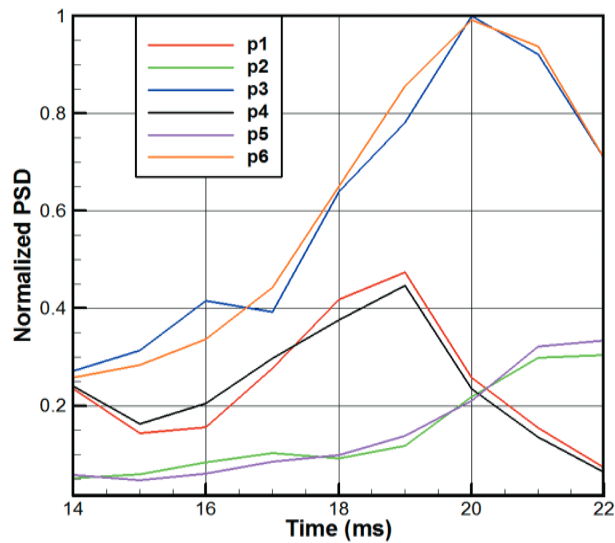
Figure 24. Case 1cp1 FFT of the pressure history on the combustion-chamber at probe p1 for the pulsing frequency 4532 Hz. ($z = 1$ cm).

30 cm combustion chamber with mixture ratio pulsing

Mixture ratio pulsation tests with frequency 2000 Hz are performed. The pulsation is applied for only two injectors which is shown in [Figure 1b](#) injector-1 and injector-6. The pulsations for the two injectors are in phase. Four different tests are performed. The first case only has pulsation applied at 10 ms. The second case has two pulsations applied at 10 ms and 16.5 ms, while the third case has three pulsations starting at 10 ms, 16.5 ms, and 21 ms. Each pulsation stops after three cycles. The fourth case applies two pulsations at 10 ms and 16.5 ms the same way as in the third case but a third pulsation at 21 ms of the same type as the third pulsation in the third case but 180 degree out of phase. The mixture ratio pulsation history is presented in [Figure 29](#).



(a) longitudinal mode



(b) tangential mode

Figure 25. Case 1cp1 peak PSD for the longitudinal and tangential modes for the pulsing frequency 4532 Hz ($z = 1$ cm).

The FFT analysis of the pressure oscillation at the probes for the three sub-cases are presented in Figure 30–32. With the first longitudinal mixture ratio pulsation, the longitudinal instability is slightly enhanced. With two longitudinal mixture ratio pulsations, the longitudinal instability is significantly increased. The longitudinal instability becomes stronger. However, the longitudinal instability amplitude is significantly

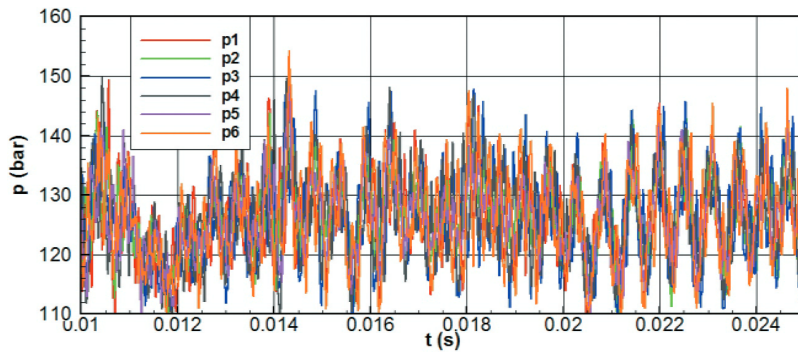


Figure 26. Case 1cp2 pressure history on the combustion-chamber wall for the pulsing frequency 3417 Hz. ($z = 1$ cm).

reduced when the third mixture ratio pulsations is applied at the 2000 Hz frequency. It might be that the third longitudinal mixture ratio pulsation is out of phase with the pressure oscillation. To test this conjecture the fourth test case is constructed where the third pulsation is now 180 degrees out of phase with that in third case. The computational results show a clear increased longitudinal instability on applying this third pulsation. It indicates that the combustion instability can be controlled by inlet-flux pulsation with a different phase. The pressure oscillation behaviors confirm the mixed tangential instability and longitudinal instability inside the combustion chamber. The FFT analysis of four 3 ms time duration window for the fourth case are present in [Figure](#)

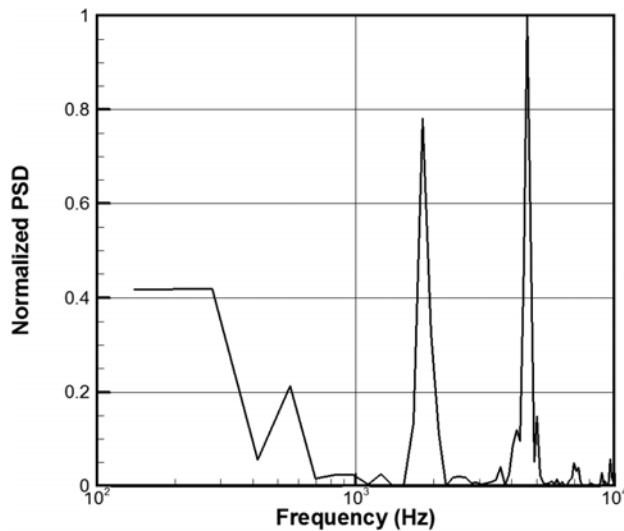
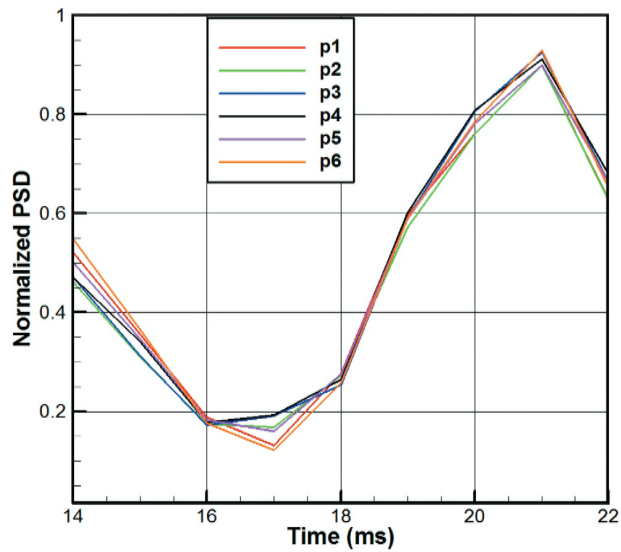
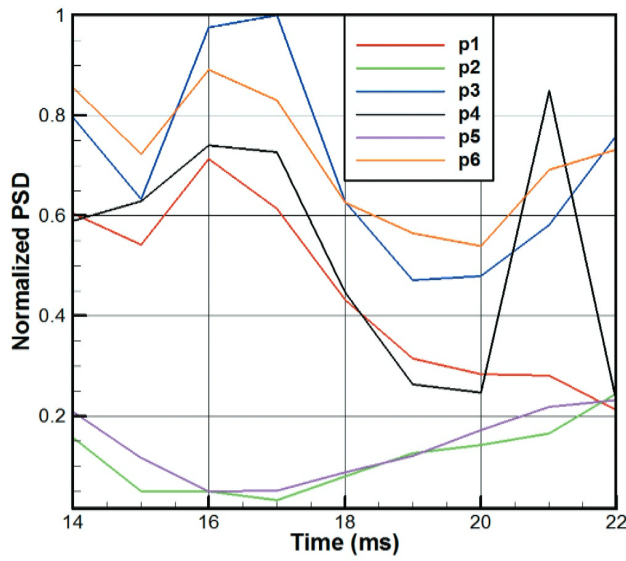


Figure 27. Case 1cp2 FFT of the Pressure history on the combustion-chamber at probe p1 for the pulsing frequency 3417 Hz. ($z = 1$ cm).



(a) longitudinal mode



(b) tangential mode

Figure 28. Case 1cp2 peak PSD for the longitudinal and tangential modes for the pulsing frequency 3417 Hz ($z = 1$ cm).

33. It clearly shows the two modes of the combustion instability alternate during the simulation time.

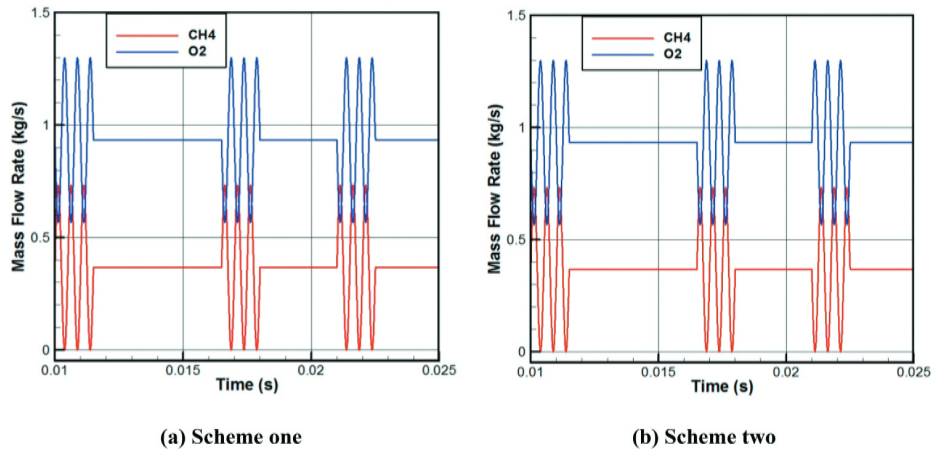


Figure 29. Mixture ratio pulsation time history.

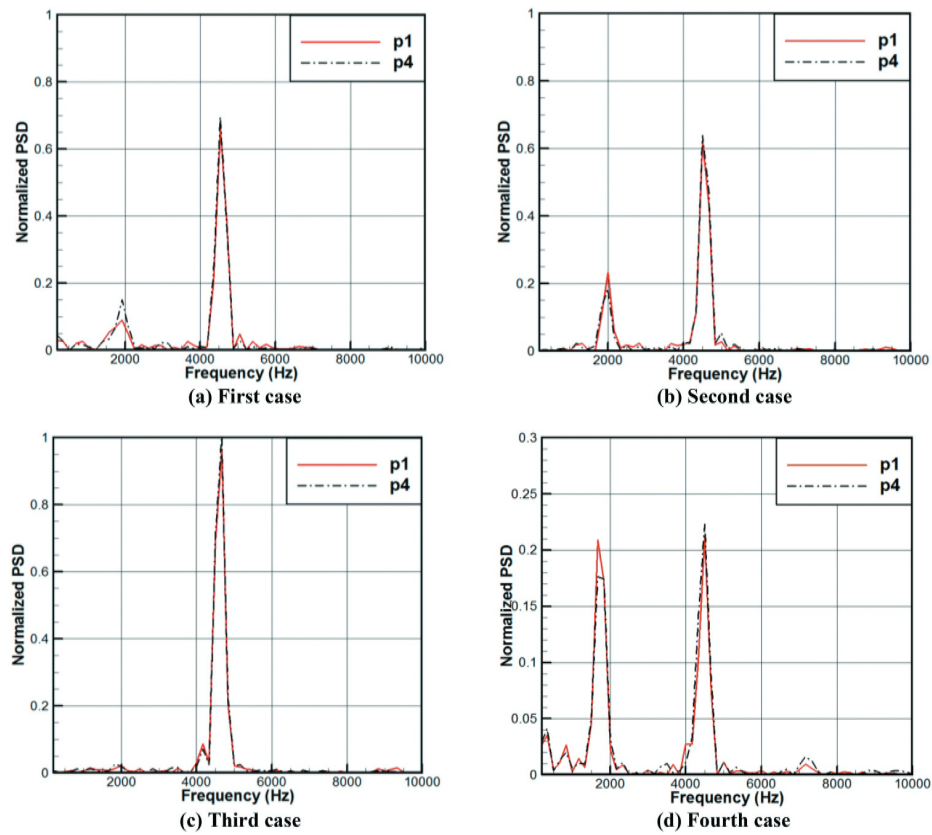


Figure 30. Case 1c FFT of pressure history on the combustion-chamber wall at probes p1 and p4 for the mixture ratio pulsing frequency 2000 Hz. ($z = 1$ cm).

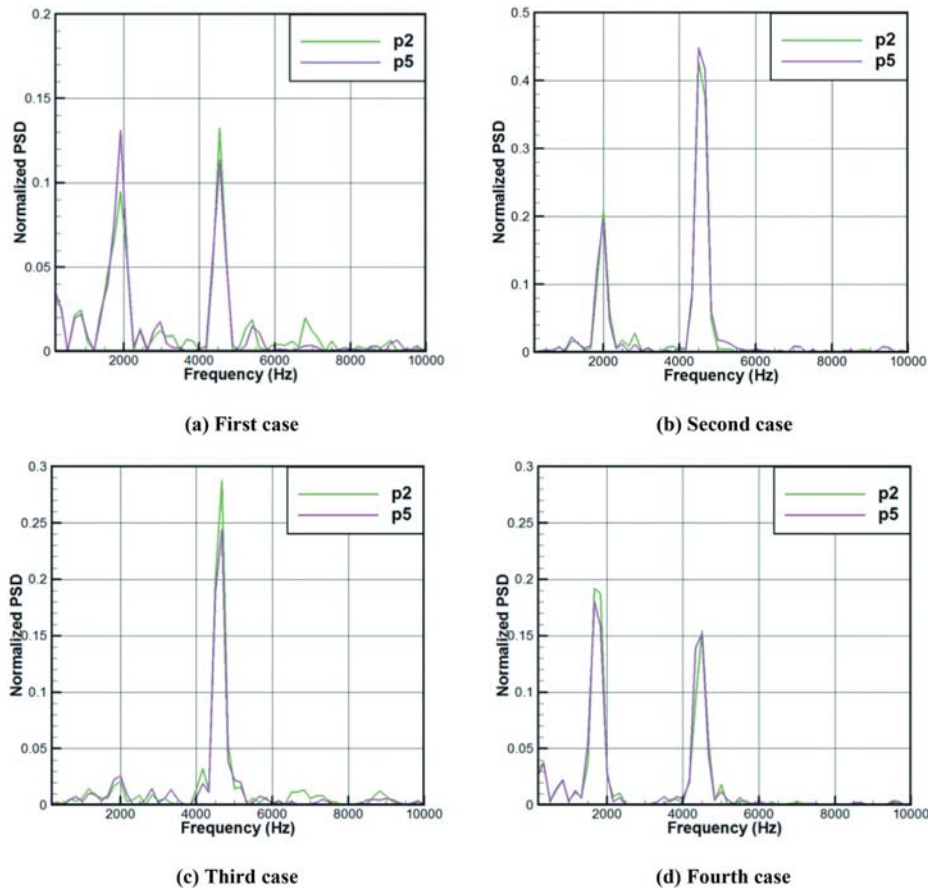


Figure 31. Case 1c FFT of pressure history on the combustion-chamber wall at probes p2 and p5 for the mixture ratio pulsing frequency 2000 Hz. ($z = 1$ cm).

Conclusions

A computational study of a rocket engine with 30 coaxial methane-oxygen injector ports, a choked nozzle, and a combustion chamber is presented. Three combustion chamber lengths 18 cm, 24 cm, and 30 cm are modeled. The 24 cm chamber is studied for three fuel-rich mixture ratio with the instability becoming more severe as the mixture becomes more fuel rich. The spontaneous longitudinal-mode and tangential-mode instabilities are observed. The strengths of the two instability modes alternate during the simulation time. The oscillation amplitudes of the two instability modes could be modified by pulsing the injector mass flux at certain pulsation frequencies.

Cases 1, 2, and 3 involved the 24 cm chamber length at three different mixture ratios. Both a first longitudinal mode at approximately 2000 Hz and a first tangential mode at about 4500 Hz for the 14.38 cm chamber diameter appeared. The amplitude of the two modes change with time. Energy appears to transfer from one mode to the

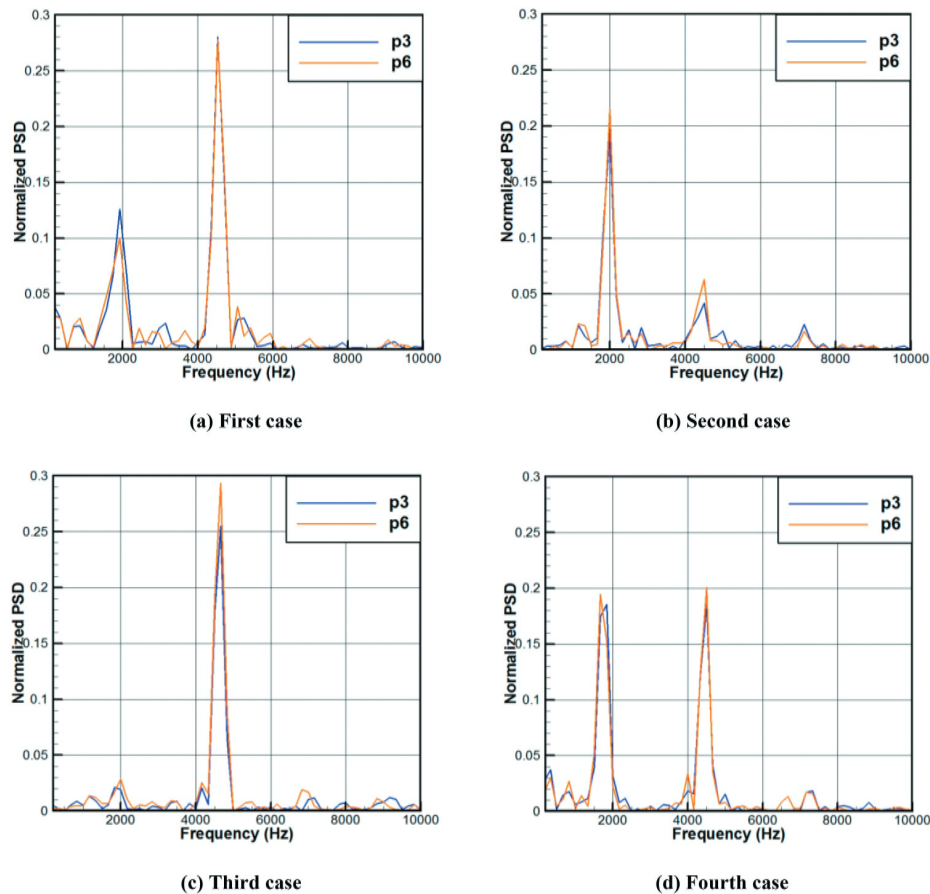


Figure 32. Case 1c FFT of pressure history on the combustion-chamber wall at probes p3 and p6 for the mixture ratio pulsing frequency 2000 Hz. ($z = 1$ cm).

other and back again such that domination alternates between the two modes. As the mixture ratio becomes less fuel rich and moves toward the stoichiometric value, the oscillation amplitude decreases, and in particular becomes noise in Case 3. This behavior is similar to the prediction of Sirignano and Crocco (1964) that was consistent with an experimental rocket motor (Bowman, Glassman, Crocco 1965) when chemical kinetics was rate-controlling. The behavior is similar to the findings of Jensen, Dodson, and Claflin (1989). Our analysis using the flame index shows that the premixed flame structures occur upstream near the injectors more commonly than the diffusion-flame structures. Consequently, the decrease in flame temperature as the mixture ratio becomes more fuel-rich results in a stronger driving mechanism for combustion instability.

The most unstable mixture ratio was applied to the 18 cm (Case 1b) and 30 cm (Case 1c) chamber lengths. For Case 1b, only the first tangential mode appeared. Both

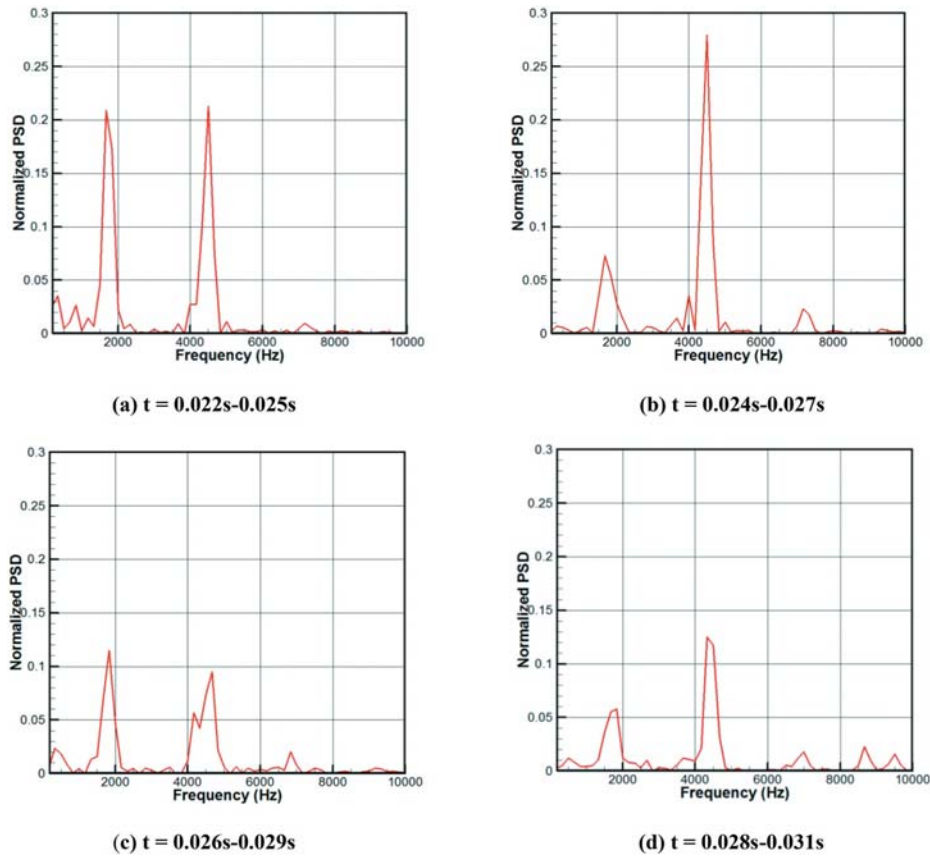


Figure 33. FFT of the pressure history at probe p1 on the combustion-chamber wall. ($z = 1$ cm).

modes appeared for Case 1 c with temporal change in the amplitudes. The first tangential mode remained dominant. Two variations of Case 1b for the 18 cm chamber were performed with pulsing at 4532 Hz in one sub-case and 3417 Hz in the other sub-case. The pulsing was performed through mass flux oscillation in the outer ring of the injectors at fixed mixture ratio. The 4532 Hz pulsing yielded a transformation of the oscillation from the pure first tangential mode to a combination of the first tangential and the first longitudinal modes. The 3417 Hz pulsing produced a low-frequency mode plus a reduced-strength first tangential mode. Secondly, pulsing in Case 1b reduced the severity of the instability. The same two pulsing variations were applied to Case 1 c for the 30 cm chamber. At pulsing of 4532 Hz, the first-tangential mode was strengthened while, at 3417 Hz, the first longitudinal mode was strengthened.

For Case 1 c, pulsing of the mixture ratio in two injectors (at constant mass flux) was done at 2000 Hz. The pulsing was repeated intermittently. The 2000 Hz pulsing tended to strengthen the longitudinal mode. The repeated pulsing had varying consequences apparently related to the phase of the pulsing with respect to the pressure

phase. It is clear from the results here that pulsing can change the mode and strength of the instability. This indicates the potential for the development of a control strategy.

Nomenclature

c_p	Specific heat at constant pressure, $J/(kg \cdot K)$
D_c	Diameter of combustor chamber, cm
D_t	Diameter of nozzle throat, cm
D_{kj}	Mass diffusivity for species k in j direction, m^2/s
E	Stagnation internal energy, J
e	Stagnation specific internal energy, J/kg
H	Stagnation internal enthalpy, J
HRR	Heat-release-rate, W
h	Specific enthalpy, J/kg
h_s	Stagnation specific enthalpy, J/kg
k	Turbulent kinetic energy, m^2/s^2
$L_{chamber}$	Length of combustion-chamber
p	Static pressure, bar
q_i	Energy flux in i th direction, $J/(m^2 \cdot s)$
R	Mixture specific gas constant, $J/(kg \cdot K)$
R_{ad}	Radius of the chamber, cm
R_{throat}	Radius of the throat, cm
u_i	Velocity components, m/s
$V_{k,i}$	Correction velocity for species k in the i th direction, m/s
T	Temperature, K
t	Time, s
W	Total molecular weight, kg/mol
W_k	Molecular weight of species k , kg/mol
X_k	Mole fraction of species k
x_i	Position, m
Y_k	Mass fraction of species k
γ	Ratio of specific heats
λ	Total thermal diffusivity, m^2/s
λ_k	Thermal diffusivity of species k , m^2/s
μ	Total dynamic viscosity, $kg/(m \cdot s)$
μ_k	Dynamic viscosity of species k , $kg/(m \cdot s)$
μ_t	Turbulent eddy viscosity, $kg/(m \cdot s)$
ν_t	Turbulent kinematic viscosity, $kg/(m \cdot s)$
ω	Specific rate of dissipation
ω_k	Reaction rate of species k , $kg/(m^3 \cdot s)$
ρ	Mass density, kg/m^3
τ_{ij}	Shear stress tensor, Pa

Acknowledgments

This research was supported by the U.S. Air Force Office of Scientific Research under grant FA9550-18-1-0392, with Dr. Mitat Birkan as the Program Manager.

Funding

This research was supported by the U.S. Air Force Office of Scientific Research under grant [FA9550-18-1-0392].

References

- Anderson, W. E., and V. Yang. 1995. Liquid rocket engine combustion instability. In *Progress in astronautics and aeronautics*, Vol. 169, 3–37. American Institute of Aeronautics and Astronautics, Reston, VA.
- Bowman, C. T., I. Glassman, and L. Crocco. 1965. Combustion instability in gas rockets. *Aiaa J.* 3 (10):1981–82. doi:10.2514/3.55206.
- Crocco, L., and S. L. Cheng. 1953. High frequency combustion instability in rockets with distributed combustion. *4th Int. Symp. Combust.* 4:865–80. doi:10.1016/S0082-0784(53)80111-6.
- Crocco, L., and S. L. Cheng. 1956. Theory of combustion instability in liquid propellant rocket motors. In *AGARD, monograph 8*, 76–162, Butterworths Science Publication, London. .
- Culick, F. E. C. 2006. Unsteady motions in combustion chambers for propulsion system. AGARDograph, AG- AVT-039, Neuilly-Sur-Seine, France.
- Harrje, D., and F. Reardon. 1972. *Liquid propellant rocket combustion instability*. NASA SP194. U.S. Government Printing Office, Washington, D.C.
- Huo, H. F., and V. Yang. 2017. Large-Eddy simulation of supercritical combustion: Model validation against gaseous H₂-O₂ injector. *J. Propuls. Power* 33 (5):1272–84. doi:10.2514/1.B36368.
- Jensen, R. J., H. C. Dodson, and S. E. Claflin 1989 LOX/hydrocarbon combustion instability investigation. NASA CR-182249
- Menon, S., and W.-H. Jou. 1991. Large-Eddy simulations of combustion instability in an axisymmetric Ramjet combustor. *Combust. Sci. Technol.* 75 (1):53–72. doi:10.1080/00102209108924078.
- Menter, F. 1994. Two-equation Eddy-viscosity turbulence models for engineering applications. *Aiaa J.* 32 (8):1598–605. doi:10.2514/3.12149.
- Miller, K., J. Sisco, N. Nugent, and W. Anderson 2005. Experimental study of combustion instabilities in a single-element coaxial swirl injector. *41st AIAA Joint Propulsion Conference*, (p. AIAA 2005–4298) doi:10.2514/6.2005-4298
- Mitchell, C. E., L. Crocco, and W. A. Sirignano. 1969. Nonlinear longitudinal instability in rocket motors with concentrated combustion. *Combust. Sci. Technol.* 1 (1):35–64. doi:10.1080/00102206908952190.
- Nguyen, T. M., P. P. Popov, and W. A. Sirignano. 2018. Longitudinal combustion instability in a rocket engine with a single coaxial injector. *J. Propuls. Power* 34 (2):354–73. doi:10.2514/1.B36516.
- Nguyen, T. M., and W. A. Sirignano. 2018. The impacts of three flamelet burning regimes in nonlinear combustion dynamics. *Combust. Flame* 195 (10):170–82. doi:10.1016/j.combustflame.2018.03.031.
- Oefelein, J. C., and V. Yang. 1993. Comprehensive review of liquid-propellant combustion instability in F-1 engines. *J. Propuls. Power* 9 (5):657–77. doi:10.2514/3.23674.
- Oefelein, J. C., and V. Yang. 1998. Modeling high-pressure mixing and combustion processes in liquid rocket engines. *J. Propuls. Power* 14 (5):843–57. doi:10.2514/2.5349.
- Poinsot, T., and D. Veynante. 2011. *Theoretical and numerical combustion*. 3rd ed. Bordeaux, France: Aquaprint.
- Popov, P. P., A. Sideris, and W. A. Sirignano. 2017. Stochastic modeling of transverse wave instability in a liquid-propellant rocket engine. *J. Fluid Mech.* 745:62–91. doi:10.1017/jfm.2014.96.
- Popov, P. P., W. A. Sirignano, and A. Sideris. 2015. Propellant injector influence on liquid-propellant rocket engine instability. *J. Propuls. Power* 31 (1):320–31. doi:10.2514/1.B35400.
- Sirignano, W. A., and L. Crocco. 1964. A shock wave model of unstable rocket combustors. *Aiaa J.* 2 (7):1285–96. doi:10.2514/3.2534.
- Sisco, J., Y. Yu, V. Sankaran, and W. Anderson. 2011. Examination of mode shapes in an unstable model rocket combustor. *J. Sound Vib.* 330 (1):61–74. doi:10.1016/j.jsv.2010.07.016.
- Strelets, M. 2001. Detached Eddy simulation of massively separated flows. *39th AIAA Aerospace Sciences Meeting*, Reno, NV (p. AIAA 2001–0879). doi:10.2514/6.2001-879
- Urbano, A., L. Selle, G. Staffelbach, B. Cuenot, T. Schmitt, S. Ducruix, and S. Candel. 2016. Exploration of combustion instability triggering using large Eddy simulation of a multiple injector liquid rocket engine. *Combust. Flame* 169:129–40. doi:10.1016/j.combustflame.2016.03.020.

- Wang, X. J., H. F. Huo, U. Unnikrishnan, and V. Yang. 2018a. A systematic approach to high fidelity modeling and efficient simulation of supercritical fluid mixing and combustion. *Combust. Flame* 195:203–15. doi:[10.1016/j.combustflame.2018.04.030](https://doi.org/10.1016/j.combustflame.2018.04.030).
- Wang, X. J., L. W. Zhang, Y. X. Li, S. T. Yeh, and V. Yang. 2018b. Supercritical combustion of gas-centered liquid-swirl coaxial injectors for staged-combustion engines. *Combust. Flame* 197:204–14. doi:[10.1016/j.combustflame.2018.07.018](https://doi.org/10.1016/j.combustflame.2018.07.018).
- Xiong, J. T., H. Morgan, J. Krieg, F. Liu, and W. A. Sirignano. 2020. Nonlinear combustion instability in a multi- injector rocket engine. *Aiaa J.* 58 (1):219–35. doi:[10.2514/1.J058036](https://doi.org/10.2514/1.J058036).
- Zinn, B. T. 1968. A theoretical study of nonlinear combustion instability in liquid-propellant rocket engines. *Aiaa J.* 6 (10):1966–72. doi:[10.2514/3.4908](https://doi.org/10.2514/3.4908).